

Supporting Information

Sulfur-resistant catalytic NO oxidation over surface-disproportionated CaMnO₃ perovskites

Xin Xu^a, Xue Bai^b, Yunpeng Zhang^{c,d}, Bolin Xia^a, Xinyu Wang^a, Sascha Ehlert^e, Leneng Yang^e, Yan Chen^{a,}, Stephan Förster^{c,d}, Rafal E. Dunin-Borkowski^b, Daiqi Ye^a, Peirong Chen^{a,*}*

^a National Engineering Laboratory for VOCs Pollution Control Technology and Equipment, Guangdong Provincial Key Laboratory of Atmospheric Environment and Pollution Control, School of Environment and Energy, South China University of Technology, 510006 Guangzhou, China.

^b Ernst Ruska-Centre for Microscopy and Spectroscopy with Electrons and Peter Grünberg Institute, Forschungszentrum Jülich, 52428 Jülich, Germany

^c Jülich Centre for Neutron Science (JCNS-1/IBI-8), Forschungszentrum Jülich, 52425 Jülich, Germany

^d Institute of Physical Chemistry, RWTH Aachen University, 52074 Aachen, Germany

^e Guangdong Chengyi Environmental Technology Corp., 512158 Shaoguan, China

*Corresponding authors. Tel.: +86(0)2039380508. E-mails: chenpr@scut.edu.cn; escheny@scut.edu.cn.

22	Catalyst Synthesis	4
23	Catalyst Activity	4
24	Figure S1.	6
25	Figure S2.	7
26	Figure S3.	8
27	Figure S4.	9
28	Figure S5.	10
29	Figure S6.	11
30	Figure S7.	12
31	Figure S8.	13
32	Figure S9.	14
33	Figure S10.	15
34	Figure S11.	16
35	Figure S12.	17
36	Figure S13.	18
37	Figure S14.	19
38	Figure S15.	20
39	Figure S16.	21
40	Figure S17.	22
41	Figure S18.	23
42	Figure S19.	24
43	Figure S20.	25
44	Figure S21.	26
45	Figure S22.	27
46	Figure S23.	28
47	Figure S24.	29
48	Figure S25.	30
49	Figure S26.	31
50	Figure S27.	32

51	Figure S28.	33
52	Figure S29.	34
53	Figure S30.	35
54	Figure S31.	36
55	Figure S32.	37
56	Table S1.	38
57	Table S2.	39
58	Table S3.	40
59	Table S4.	41
60	References	42
61		

62 **Catalyst Synthesis**

63 CaCO_3 and MnCO_3 were dissolved in a 1.5 M HNO_3 solution in a 1:1 molar ratio,
64 followed by the addition of an $(\text{NH}_4)_2\text{CO}_3$ solution at a $(\text{Ca}^{2+} + \text{Mn}^{2+})/\text{CO}_3^{2-}$ molar ratio
65 of 1:2.5. The mixture was stirred for 30 min, then the precipitate was centrifuged and
66 dried under vacuum at 80 °C for 12 hours. The dried powder was calcined at 900 °C for
67 5 hours in air flow in a muffle furnace. The sample was denoted CMO.

68 **Catalyst Activity**

69 **CO oxidation.** Catalytic activity in CO oxidation was evaluated using 50 mg of
70 catalyst (40–60 mesh) in a fixed-bed quartz tubular microreactor ($\Phi=10.0$ mm). The
71 gas composition was 3000 ppm CO + 10 vol % O_2 + balance N_2 , with a total gas flow
72 rate of approximately $200 \text{ mL}\cdot\text{min}^{-1}$ and a WHSV of *ca.* $120,000 \text{ mL}\cdot\text{h}^{-1}\cdot\text{g}^{-1}$. A gas
73 chromatography (GC-2014, Shimadzu) was used for online detection of the outlet
74 concentrations of CO and CO_2 . The CO conversion ($X_{\text{CO},\%}$) was calculated using Eq.
75 S1, where C_{in} and C_{out} are the CO concentrations corresponding to the inlet and outlet,
76 respectively.

$$77 \quad X_{\text{CO}} = \frac{C_{\text{in}} - C_{\text{out}}}{C_{\text{in}}} \times 100\% \quad (\text{S1})$$

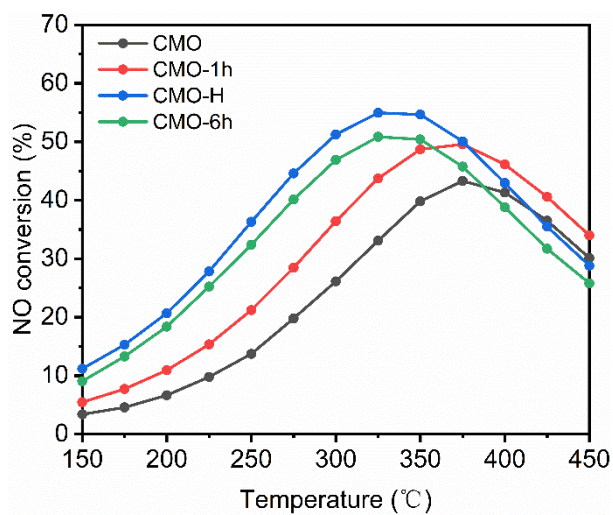
78 **CO+C₃H₆ oxidation and CO+C₃H₆+NO oxidation.** Catalytic activity was
79 evaluated using 50 mg of catalyst (40–60 mesh) in a fixed-bed quartz tubular
80 microreactor ($\Phi=10.0$ mm). The composition of the experimental reaction gas was 3000
81 ppm CO + 1000 ppm C_3H_6 + 500 ppm NO (when needed) + 10 vol % O_2 + balance N_2 ,
82 with a total gas flow rate of about $200 \text{ mL}\cdot\text{min}^{-1}$, and a WHSV of about $120,000$
83 $\text{mL}\cdot\text{h}^{-1}\cdot\text{g}^{-1}$. The concentrations of products and reactants were monitored online using

84 an MKS Multigas 2030 FTIR spectrometer. The conversion rates of NO (X_{NO} , %), CO
85 (X_{CO} , %) or C₃H₆ ($X_{\text{C}_3\text{H}_6}$, %) were calculated by the following Eq. S2, where C_{in} and
86 C_{out} are the concentrations of NO, CO, or C₃H₆ at the inlet and outlet, respectively.

87
$$X_{\text{NO,CO or C}_3\text{H}_6} = \frac{C_{\text{in}} - C_{\text{out}}}{C_{\text{in}}} \times 100\% \quad (\text{S2})$$

88

89

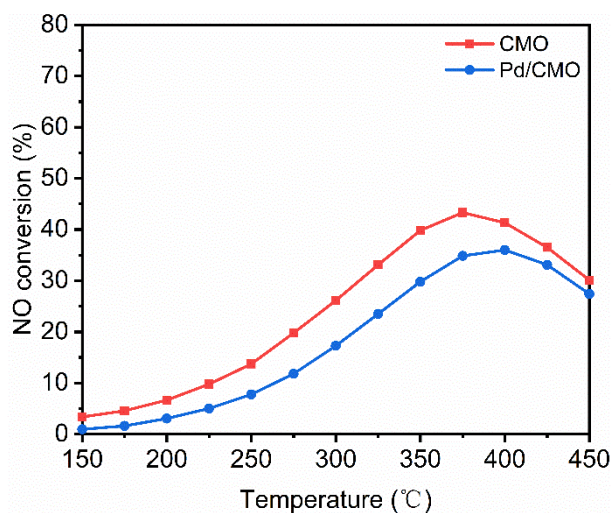


90

91 **Figure S1.** NO conversion as a function of temperature over the CMO, CMO-1h, CMO-
92 H, and CMO-6h catalysts. Gas condition: 500 ppm NO, 10 vol % O₂, and N₂ balance;
93 200 mL·min⁻¹ in total.

94

95

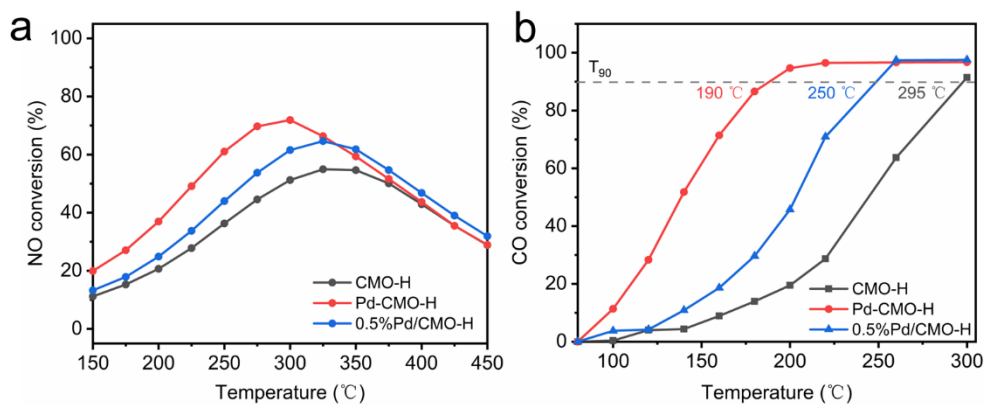


96

97 **Figure S2.** NO conversion as a function of temperature over the CMO, and Pd/CMO
98 catalysts. Gas condition: 500 ppm NO, 10 vol % O₂, and N₂ balance; 200 mL·min⁻¹ in
99 total.

100

101

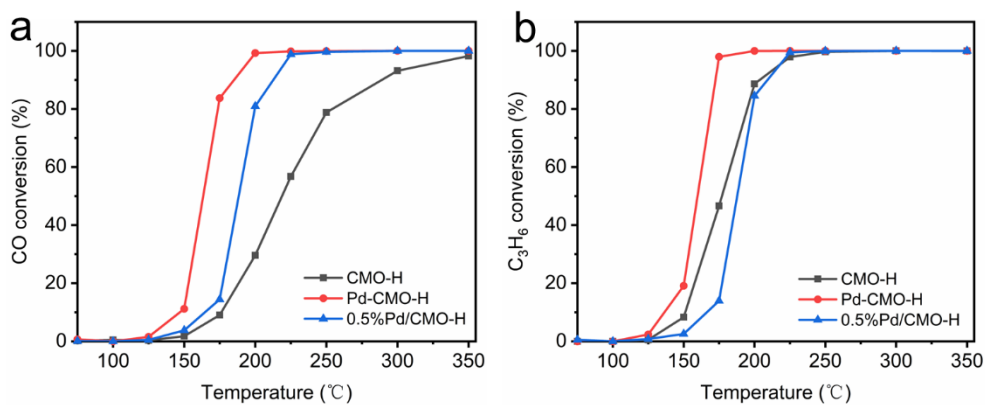


102

103 **Figure S3.** (a) NO and (b) CO conversion as a function of temperature over the CMO-
 104 H, Pd-CMO-H (with 0.2% Pd doping), and 0.5%Pd/CMO-H catalysts. Gas conditions:
 105 (a) 500 ppm NO, 10 vol % O₂, and N₂ balance; (b) 3000 ppm CO, 10 vol % O₂, and N₂
 106 balance; 200 mL·min⁻¹ in total.

107

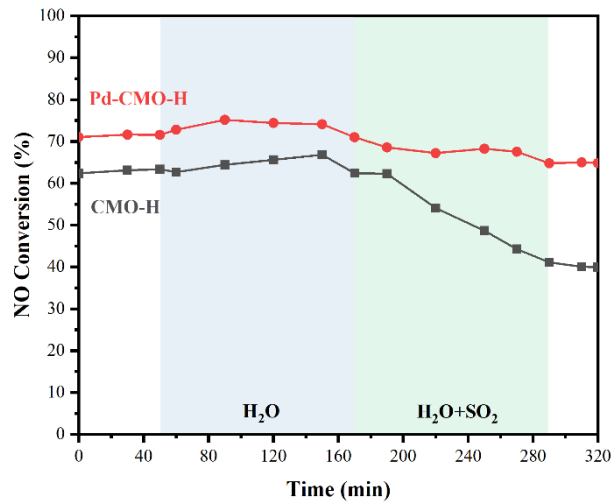
108



109

110 **Figure S4.** (a) CO and (b) C₃H₆ conversion as a function of temperature for CMO-H,
 111 Pd-CMO-H, and 0.5%Pd/CMO-H in CO+C₃H₆ co-oxidation. Gas condition: 3000 ppm
 112 CO, 1000 ppm C₃H₆, 10 vol % O₂, and balance N₂; 200 mL·min⁻¹ in total.

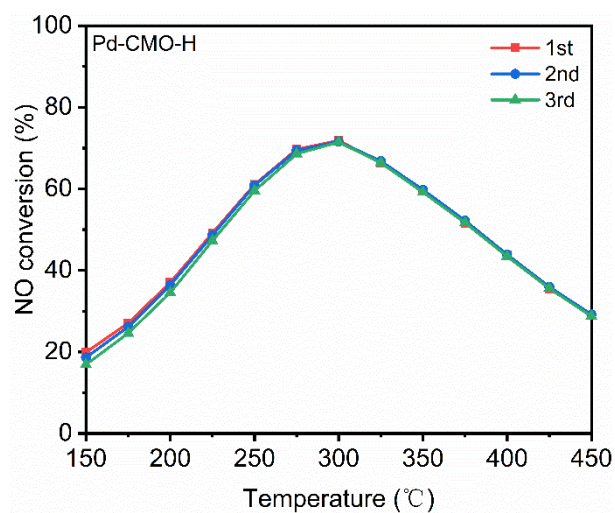
113



114

115 **Figure S5.** Prolonged NO oxidation tests over CMO-H and Pd-CMO-H at 325 °C and
 116 300 °C, respectively. Reaction condition: 500 ppm NO, 10% O₂, 8 ppm SO₂ (when
 117 added), 5 vol % H₂O vapor (when added), and balance N₂.

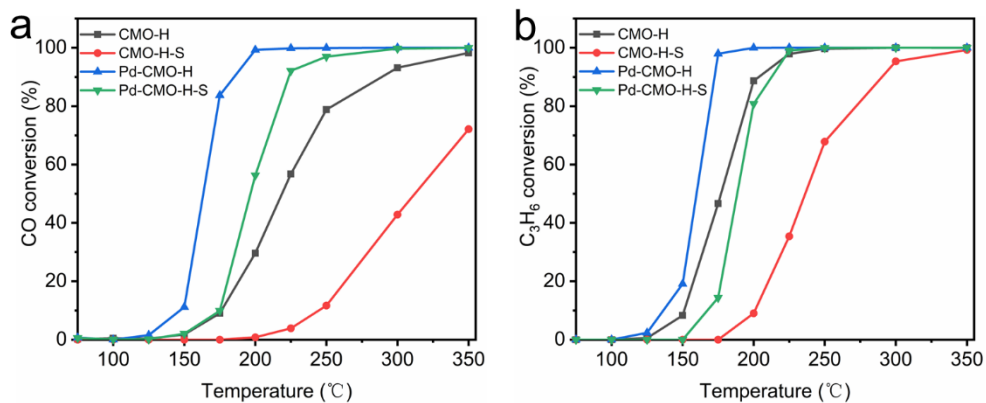
118



119

120 **Figure S6.** Catalytic performance of Pd-CMO-H in three consecutive cycles of NO
121 oxidation. Gas condition: 500 ppm NO, 10 vol % O₂, and N₂ balance; 200 mL·min⁻¹ in
122 total.

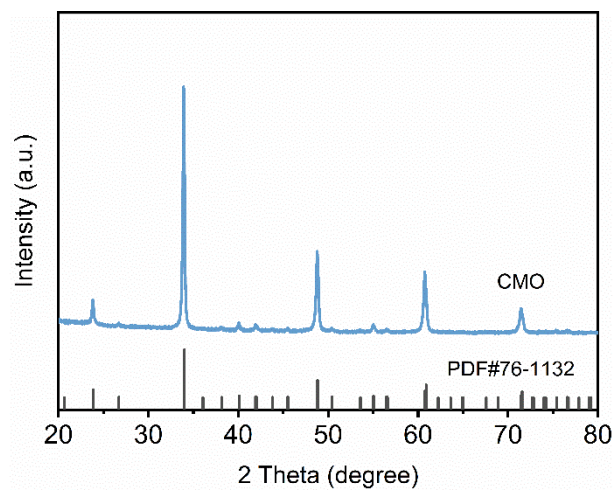
123



124

125 **Figure S7.** (a) CO and (b) C₃H₆ conversion as a function of temperature for different
 126 CMO catalysts in CO+C₃H₆ co-oxidation. Gas condition: 3000 ppm CO, 1000 ppm
 127 C₃H₆, 10 vol % O₂, and balance N₂; 200 mL·min⁻¹ in total.

128

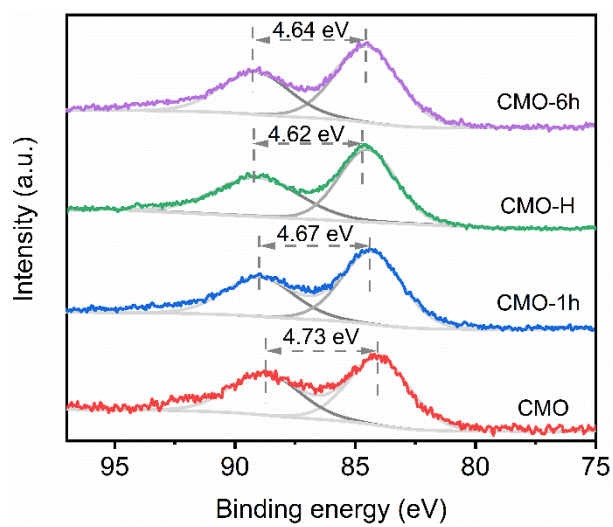


129

130

131

Figure S8. XRD pattern for CMO.



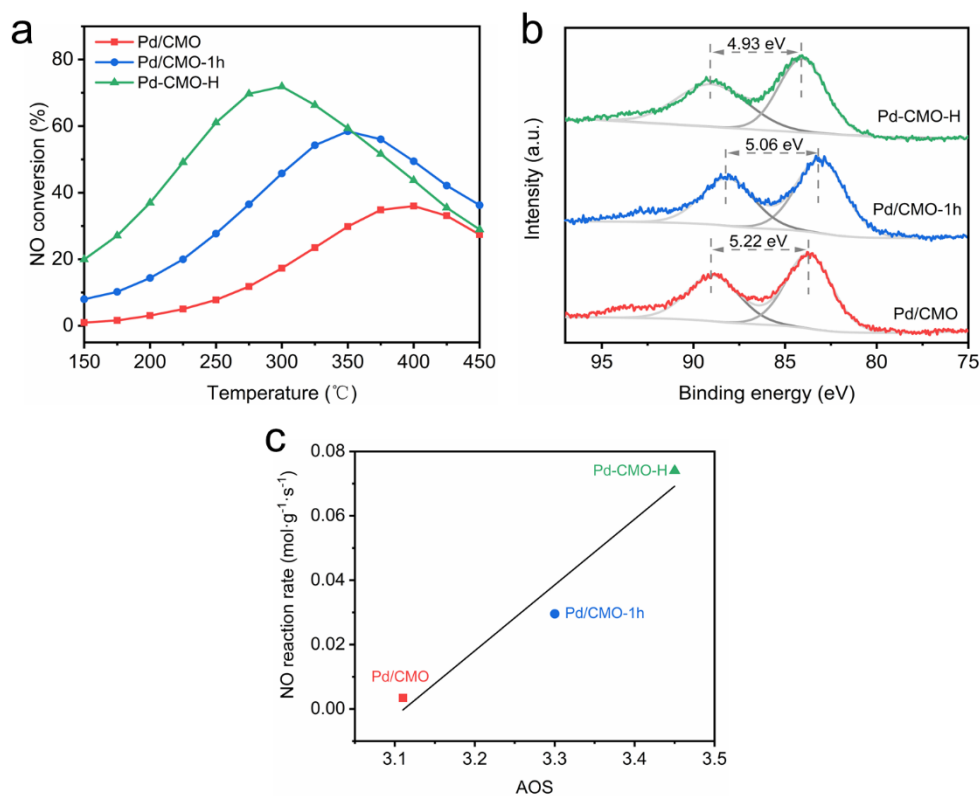
132

133

Figure S9. XP Mn 3s spectra for CMO, CMO-1h, CMO-H and CMO-6h.

134

135



136

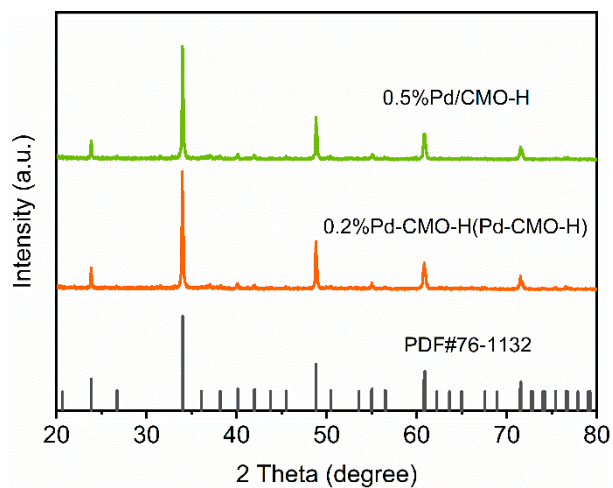
137 **Figure S10.** (a) NO conversion vs. temperature curves, and (b) XP Mn 3s spectra for
 138 Pd/CMO, Pd/CMO-1h and Pd-CMO-H; (c) correlation between the AOS of surface Mn
 139 and the NO reaction rate at 150 °C for different Pd-loaded perovskites. Gas condition:
 140 (a) 500 ppm NO, 10 vol % O₂, and balance N₂; 200 mL·min⁻¹ in total.

141

142 **Note:**

143 The ΔE values of Pd/CMO, Pd/CMO-1h and Pd-CMO-H were measured to be 5.22 eV,
 144 5.06 eV and 4.93 eV (Figure S12b), corresponding to AOS values of 3.11, 3.30 and
 145 3.45, respectively.

146

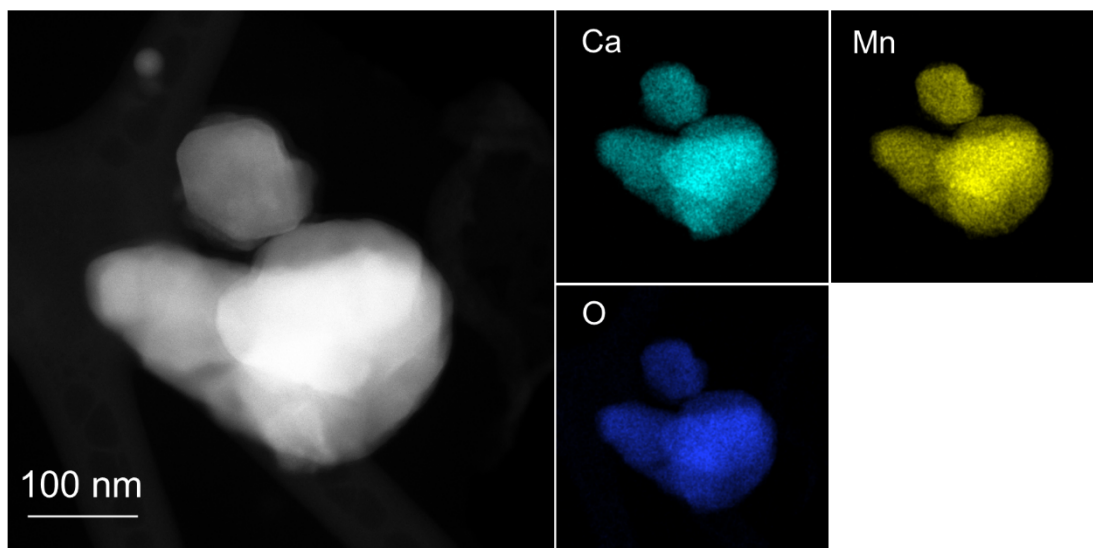


147

148 **Figure S11.** XRD patterns for Pd-CMO-H with 0.2 wt % and 0.5wt % Pd content.

149

150



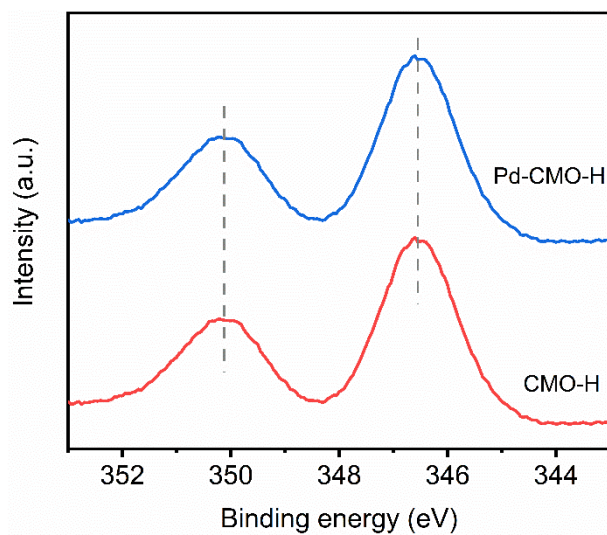
151

152 **Figure S12.** Aberration-corrected HAADF-STEM image with STEM-EDS element

153 mappings for CMO-H.

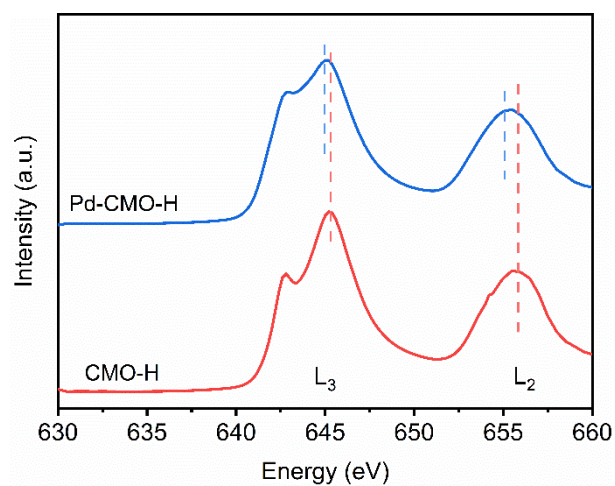
154

155



156
157
158
159

Figure S13. XP Ca 2p spectra for CMO-H and Pd-CMO-H.



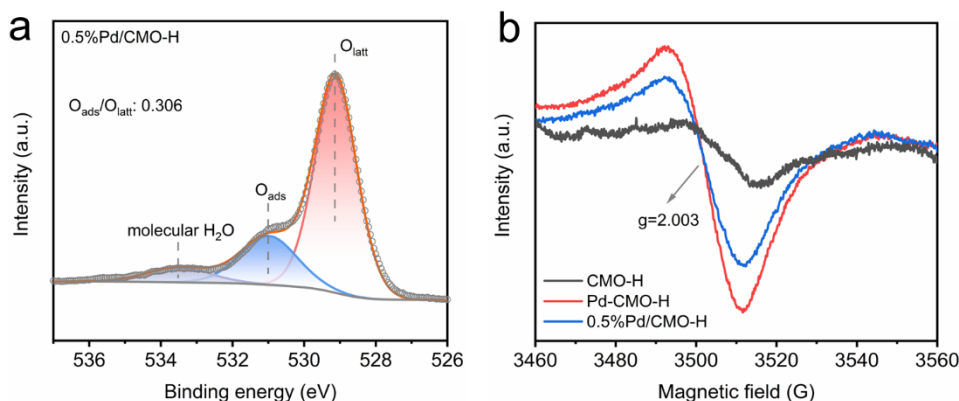
160

161

Figure S14. Mn *L*-edge absorption spectra of CMO-H and Pd-CMO-H

162

163



164

165 **Figure S15.** (a) O 1s XPS of 0.5%Pd/CMO-H; (b) EPR results over CMO-H, Pd-
 166 CMO-H, 0.5%Pd/CMO-H.

167

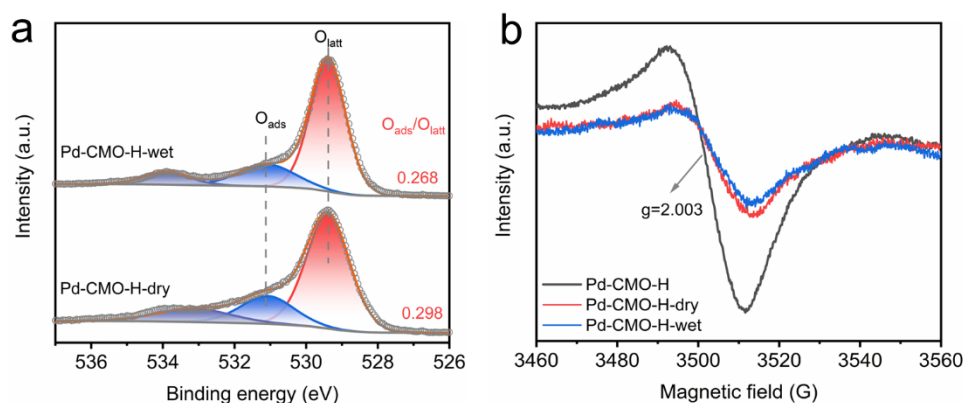
168

169

170 **Note:**

171 Compared to Pd-CMO-H (0.318), the ratio of O_{ads}/O_{latt} for 0.5%Pd/CMO-H (0.306) has
 172 decreased, indicating a reduced amount of oxygen vacancies. This conclusion is
 173 supported by EPR, which shows that the signal at g=2.003 for oxygen vacancies
 174 decreased more significantly in 0.5%Pd/CMO-H compared to Pd-CMO-H. In summary,
 175 0.5%Pd/CMO-H has fewer oxygen vacancies than Pd-CMO-H, leading to a decline in
 176 its catalytic activity. Furthermore, through EPR results, we also found that Pd-CMO-H
 177 has the highest number of oxygen vacancies, followed by 0.5%Pd/CMO-H, with CMO-
 178 H having the least. This observation is consistent with the activity-oxygen vacancy
 179 correlation revealed in Figure 6d.

180



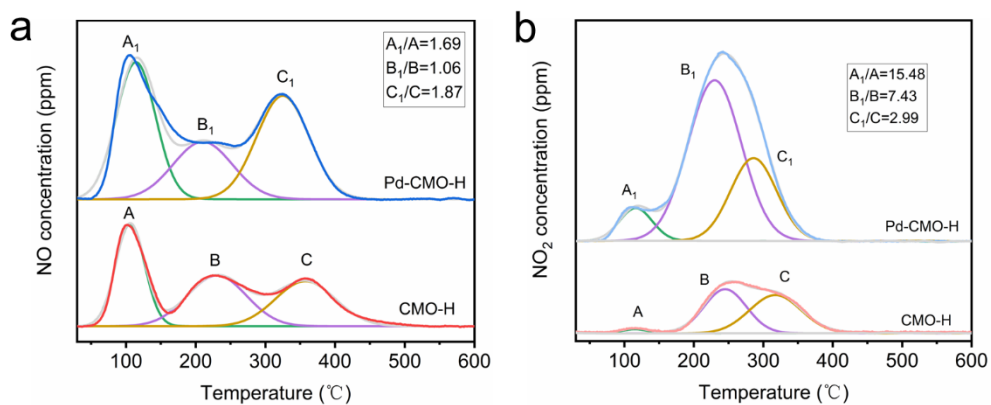
181

182 **Figure S16.** (a) XP O 1s spectra for Pd-CMO-H-dry and Pd-CMO-H-wet; (b) EPR results
 183 over Pd-CMO-H, Pd-CMO-H-dry and Pd-CMO-H-wet. Pd-CMO-H-dry refers to the fresh
 184 catalyst after NO oxidation without water vapor; Pd-CMO-H-wet refers to the fresh
 185 catalyst after NO oxidation with water vapor.

186

187 **Note:**

188 The $O_{\text{ads}}/O_{\text{latt}}$ ratio for Pd-CMO-H decreased from 0.318 (Table 1) to 0.298 (Figure S18a)
 189 after NO oxidation reaction (Pd-CMO-H-dry), corresponding to a decreased content of
 190 oxygen vacancies. The consumption of oxygen vacancies can be attributed their
 191 involvement in the reaction, presumably as intermediate oxidants.[S1] After NO
 192 oxidation in the presence of water vapor, the $O_{\text{ads}}/O_{\text{latt}}$ decreased further to 0.268 (Pd-
 193 CMO-H-wet, Figure S15a), likely due to a consumption of oxygen vacancy by H₂O
 194 molecules. This assumption was confirmed by EPR studies (Figure S15b). Specifically,
 195 the signal at $g=2.003$ for oxygen vacancies decreased more significantly after NO
 196 oxidation reaction under wet conditions (Pd-CMO-H-wet) than under dry conditions
 197 (Pd-CMO-H-dry). As a whole, one can conclude that H₂O molecules can consume the
 198 oxygen vacancies that are active in oxidation reactions and, consequently, decreased
 199 the catalytic activity in NO oxidation with water vapor.

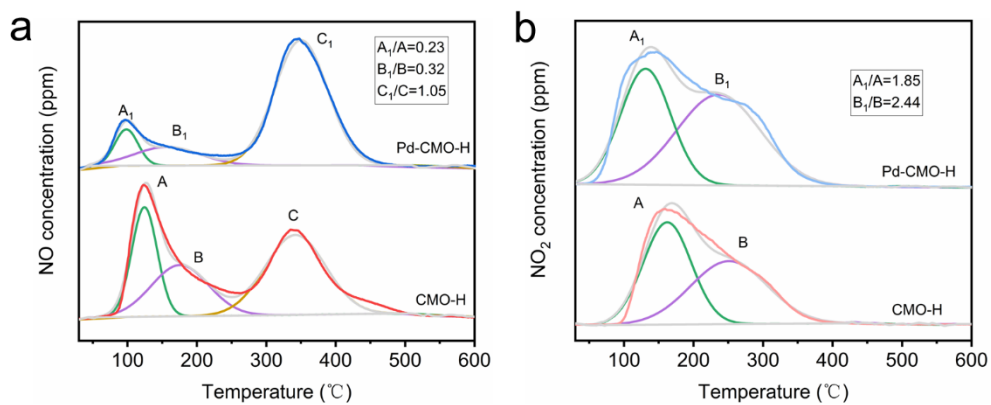


200

201 **Figure S17.** NO (a) and NO₂ (b) concentration profiles during NO-TPD for CMO-H

202 and Pd-CMO-H.

203

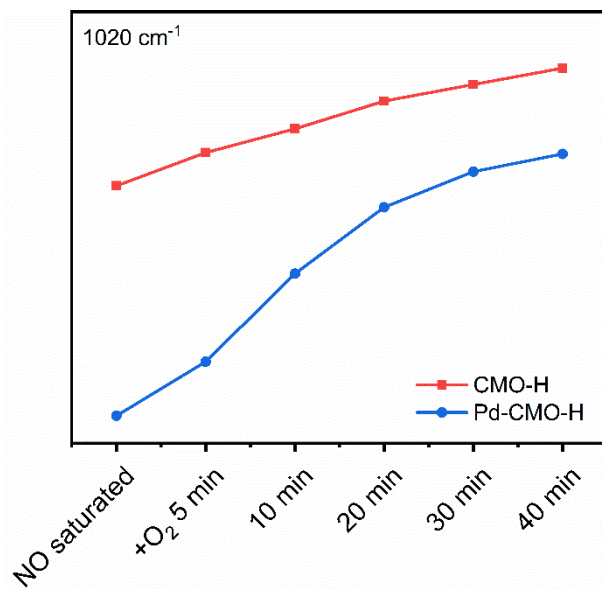


204

205 **Figure S18.** Deconvoluted NO (a) and NO₂ (b) concentration profiles during NO+O₂-

206 TPD.

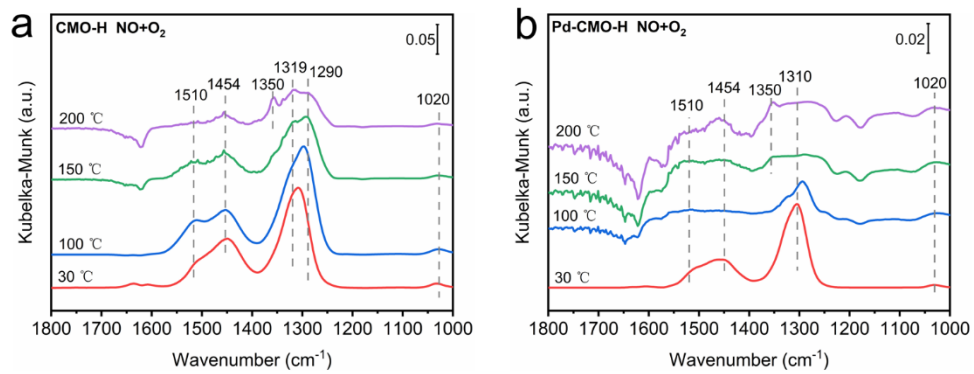
207



208

209 **Figure S19.** Normalized intensities of the IR band at 1020 cm⁻¹ over NO-saturated
210 catalysts during subsequent O₂ exposure.

211

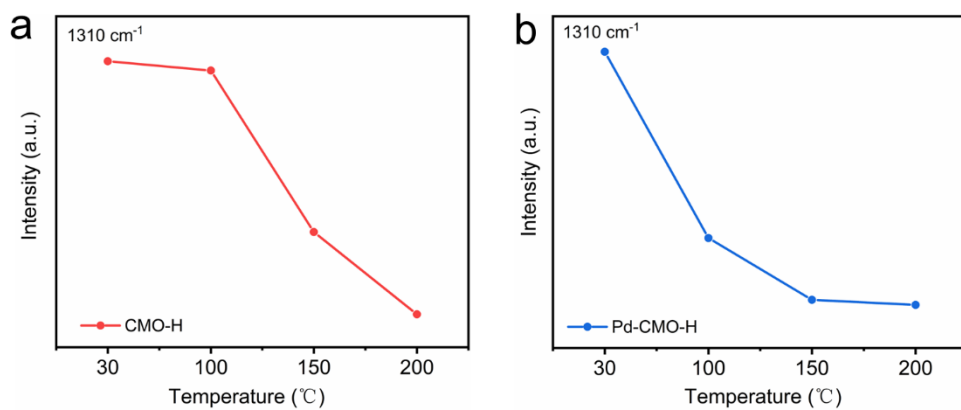


212

213 **Figure S20.** *In situ* DRIFT spectra for (a) CMO-H and (b) Pd-CMO-H during exposure

214 in a NO+O₂ mixture at different temperatures.

215



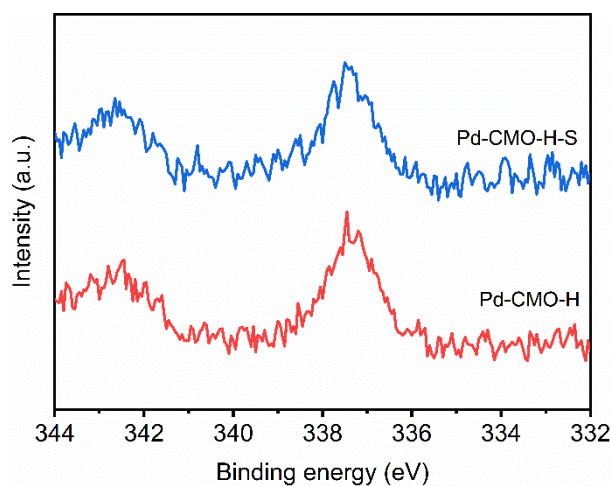
216

217 **Figure S21.** Temperature-dependent change of the IR band intensity at 1310 cm⁻¹

218 over (a) CMO-H and (b) Pd-CMO-H.

219

220



221

222

Figure S22. XP Pd 3d spectra of Pd-CMO-H and Pd-CMO-H-S.

223

224 **Note:**

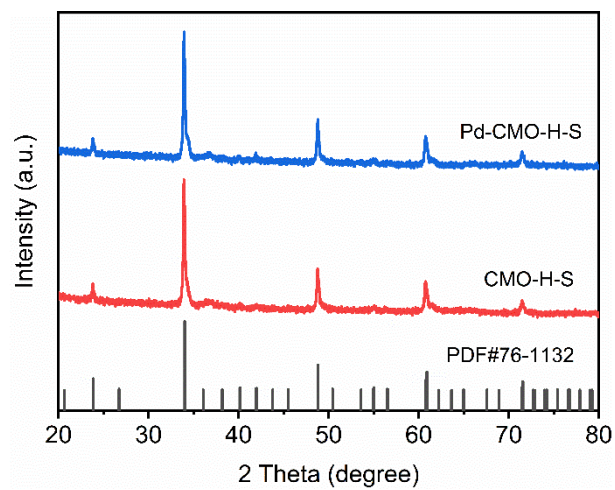
225 There was no change in the binding energy position of Pd 3d_{5/2} between the Pd-CMO-

226 H and Pd-CMO-H-S catalysts, suggesting that sulfur-poisoning treatment did not

227 change the Pd valence. The binding energy of Pd⁰ is 335.1-335.4 eV and that of Pd²⁺ is

228 336.1-337.9 eV.[S2, 3] Therefore, Pd species are present as Pd²⁺ or PdO in the catalysts.

229

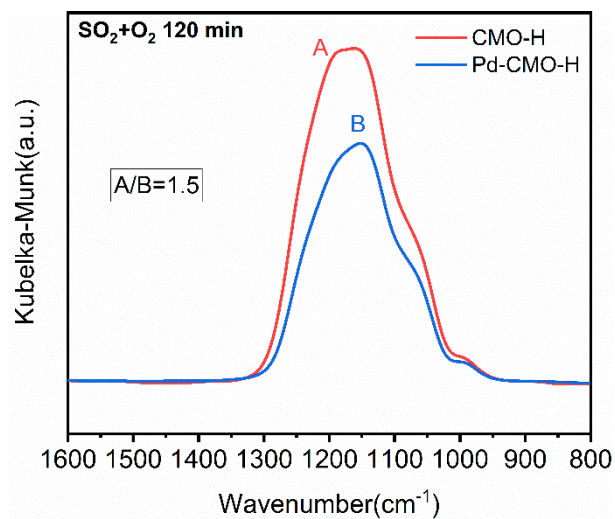


230

231

232

Figure S23. XRD patterns of CMO-H-S, and Pd-CMO-H-S.

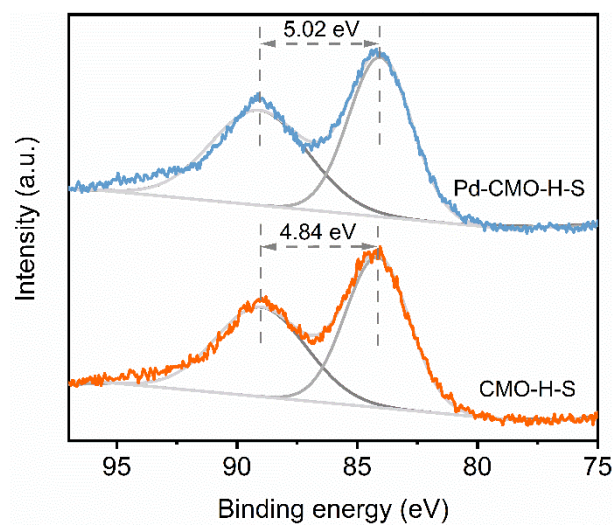


233

234 **Figure S24.** *In situ* DRIFT spectra during SO₂ poisoning over CMO-H, and Pd-CMO-

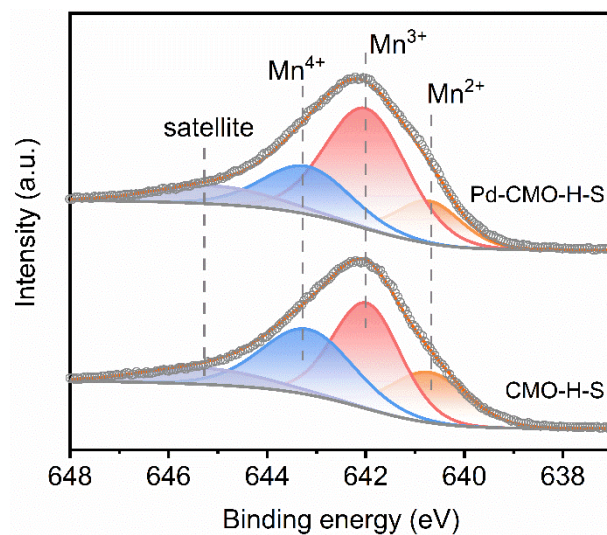
235 H at 120 min.

236



237
238
239

Figure S25. Mn 3s XPS for CMO-H-S, and Pd-CMO-H-S.

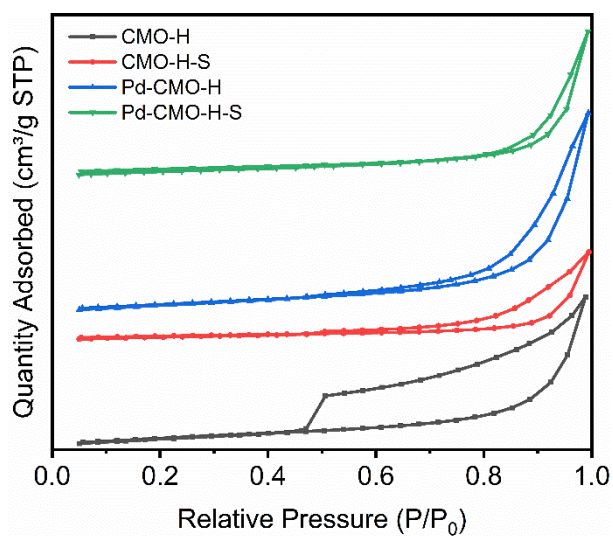


240

241

242

Figure S26. Mn 2*p* XPS for CMO-H-S, and Pd-CMO-H-S.

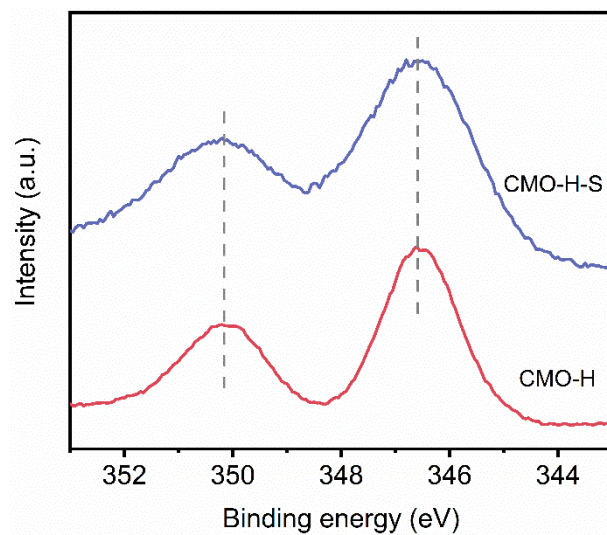


243

244 **Figure S27.** N₂-adsorption/desorption isotherms of CMO-H, CMO-H-S, Pd-CMO-H,

245 and Pd-CMO-H-S.

246

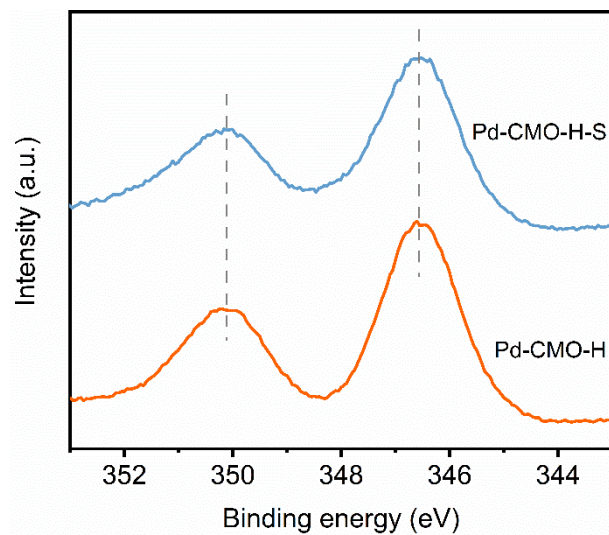


247

248

249

Figure S28. Ca 2p XPS for CMO-H, and CMO-H-S.

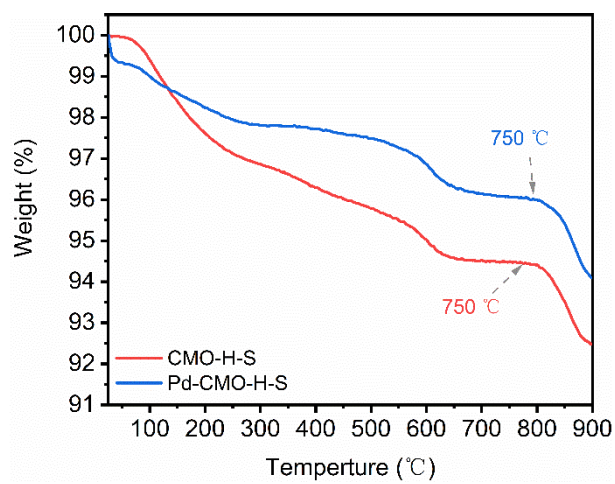


250

251

252

Figure S29. Ca 2*p* XPS for Pd-CMO-H, and Pd-CMO-H-S.

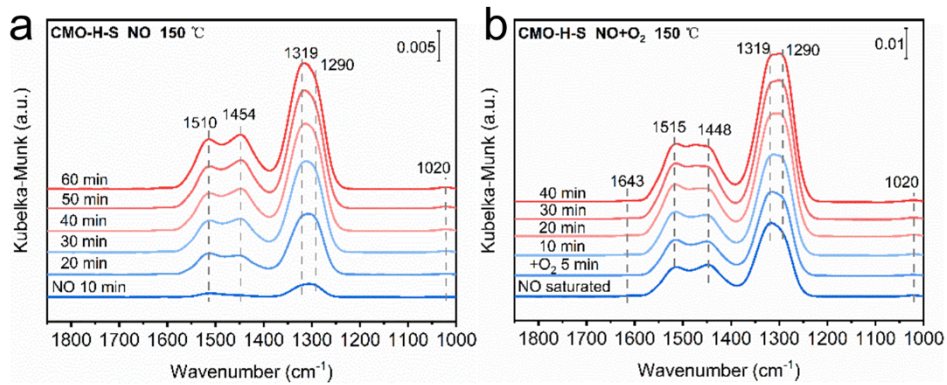


253

254

255

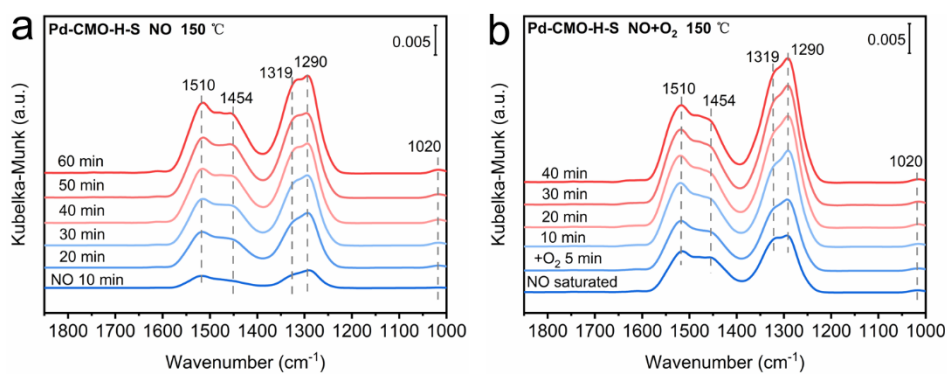
Figure S30. TG curves of CMO-H-S, and Pd-CMO-H-S.



256

257 **Figure S31.** *In situ* DRIFT spectra during NO oxidation over (a) CMO-H-S, and (b) O₂

258 addition to the NO-saturated CMO-H-S.



259

260 **Figure S32.** *In situ* DRIFT spectra during NO oxidation over (a) Pd-CMO-H-S, and

261 (b) O₂ addition to the NO-saturated Pd-CMO-H-S.

262

263 **Table S1.** Comparison of NO oxidation performance of the Pd-CMO-H catalyst with
264 those in literature

Sample	Pd content	Reaction conditions	Max. NO conversion	Ref.
Pd-CMO-H	0.2 wt %	500 ppm NO, 10% O ₂	71%	—
Pd/Al ₂ O ₃	1 wt %	500 ppm NO, 8% O ₂	62%	[S4]
Pt-Pd/Al ₂ O ₃	0.32 wt %	600 ppm NO, 8% O ₂	60%	[S5]
Pd/Al ₂ O ₃	2.3 wt %	500 ppm NO, 8% O ₂	65%	[S6]

265

266

Table S2. Quantitative XPS data of CMO and CMO-H

Sample	Ca (wt %)	Mn (wt %)
CMO	15.74	14.40
CMO-H	4.52	18.05

267

268

269

Table S3. Quantitative XPS data of CMO, CMO-1h, CMO-H, and CMO-6h.

Sample	Mn ⁴⁺ /Mn ³⁺	ΔE	AOS
CMO	0.76	4.73	3.69
CMO-1h	0.80	4.67	3.76
CMO-H	1.02	4.62	3.82
CMO-6h	0.89	4.64	3.79

270

271

272 **Table S4.** Crystal plane spacings (d values) of CMO-H and Pd-CMO-H by SAED and
 273 in the PDF card references

Sample	Crystal plane	d value by SAED (nm)	Referenced d value (nm)
CMO-H	$(1\bar{2}1)$	0.277	0.263
	$(0\bar{4}2)$	0.160	0.152
	$(\bar{1}\bar{2}1)$	0.278	0.263
	$(\bar{2}01)$	0.276	0.222
	$(0\bar{2}1)$	0.325	0.304
Pd-CMO-H	$(\bar{1}\bar{2}1)$	0.286	0.263
	$(\bar{1}00)$	0.568	0.528
	$(\bar{1}\bar{2}\bar{1})$	0.279	0.263

274
 275

276 **References**

- 277 [S1] F. Lin, Z. Wang, J. Shao, D. Yuan, Y. He, Y. Zhu, K. Cen, Catalyst tolerance to SO₂
278 and water vapor of Mn based bimetallic oxides for NO deep oxidation by ozone,
279 RSC Adv., 7 (2017) 25132-25143. <https://doi.org/10.1039/c7ra04010e>.
- 280 [S2] A. Eyssler, P. Mandaliev, A. Winkler, P. Hug, O. Safonova, R. Figi, A. Weidenkaff,
281 D. Ferri, The Effect of the State of Pd on Methane Combustion in Pd-Doped
282 LaFeO₃, J. Phys. Chem. C, 114 (2010) 4584-4594.
283 <https://doi.org/10.1021/jp911052s>.
- 284 [S3] H. Xu, L. Tan, H. Cui, M. Xu, Y. Xiao, H. Wu, H. Dong, X. Liu, G. Qiu, J. Xie,
285 Characterization of Pd(II) biosorption in aqueous solution by *Shewanella*
286 *oneidensis* MR-1, J. Mol. Struct., 255 (2018) 333-340.
287 <https://doi.org/10.1016/j.molliq.2018.01.168>.
- 288 [S4] X. Auvray, L. Olsson, Stability and activity of Pd-, Pt- and Pd-Pt catalysts
289 supported on alumina for NO oxidation, Appl. Catal., B, 168–169 (2015) 342-352.
290 <https://doi.org/10.1016/j.apcatb.2014.12.035>
- 291 [S5] M. Kaneeda, H. Iizuka, T. Hiratsuka, N. Shinotsuka, M. Arai, Improvement of
292 thermal stability of NO oxidation Pt/Al₂O₃ catalyst by addition of Pd, Appl. Catal.,
293 B, 90 (2009) 564-569. <https://doi.org/10.1016/j.apcatb.2009.04.011>
- 294 [S6] A.B. Arvajová, P. Boutikos, R. Pečinka, P. Kočí, Global kinetic model of NO
295 oxidation on Pd/γ-Al₂O₃ catalyst including PdO formation and reduction by CO
296 and C₃H₆, Appl. Catal., B, 260 (2020) 118141.
297 <https://doi.org/10.1016/j.apcatb.2019.118141>
298